Geophysical Prospecting, 2009, 57, 463–478 doi: 10.1111/j.1365-2478.2008.00763.x

New advances in regularized inversion of gravity and electromagnetic data

Michael S. Zhdanov*

Department of Geology and Geophysics, University of Utah, 135 South 1460 East, Rm 719, Salt Lake City, UT 84112, USA

Received December 2007, revision accepted April 2008

ABSTRACT

The interpretation of potential and electromagnetic fields observed over 3D geological structures remains one of the most challenging problems of exploration geophysics. In this paper I present an overview of novel methods of inversion and imaging of gravity and electromagnetic data, which are based on new advances in the regularization theory related to the application of special stabilizing functionals, which allow the reconstruction of both smooth images of the underground geological structures and models with sharp geological boundaries. I demonstrate that sharp-boundary geophysical inversion can improve the efficiency and resolution of the inverse problem solution. The methods are illustrated with synthetic and practical examples of the 3D inversion of potential and electromagnetic field data.

INTRODUCTION

The inversion of geophysical data is complicated by the fact that geophysical data are invariably contaminated by noise and are acquired at a limited number of observation points. As a result, the solutions are ambiguous and unstable. Therefore, the inversion of geophysical data represents a typical ill-posed problem. The solution of an ill-posed problem requires the application of corresponding regularization methods (Tikhonov and Arsenin 1977). The traditional way to implement regularization in the solution of an inverse problem is based on a consideration of the class of inverse models with a smooth distribution of the model parameters. Within the framework of classical Tikhonov regularization, one can select a smooth solution by introducing the corresponding minimum norm, or 'smoothing' stabilizing functionals. This approach is widely used in geophysics and has proven to be a powerful tool for the stable inversion of geophysical data.

The traditional inversion algorithms providing smooth solutions for geological structures have difficulties, however, in describing the sharp boundaries between different geological formations. This problem arises, for example, in the inversion of a local conductive target with sharp boundaries between the conductor and the resistive host rocks, which is a typical model in the exploration for a mining target. A similar problem arises, for example, in the inversion ofr a local resistive target with sharp boundaries between the conductive formations of sea-bottom sediments and a resistive hydrocarbon reservoir, which is a typical model in offshore petroleum exploration. In these situations it can be useful to search for a stable solution within the class of inverse models with sharp petrophysical boundaries.

The mathematical technique for solving this problem is described in detail in the monograph by Zhdanov (2002). It is based on introducing a special type of stabilizing functionals, the so-called minimum support or minimum gradient support functionals (Portniaguine and Zhdanov 1999). This technique is called a focusing regularized inversion to distinguish it from the traditional smooth regularized inversion. In this paper I present an overview of new advances in the regularized inversion of gravity and electromagnetic data developed by the Consortium for Electromagnetic Modeling and Inversion (CEMI) over the last few years. I will also discuss the application of the focusing inversion to the solution of gravity and electromagnetic (EM) inverse problems.

*E-mail: mzhdanov@mines.utah.edu

© 2009 European Association of Geoscientists & Engineers

FOCUSING INVERSION

In a general case, the geophysical inverse problem can be expressed by an operator equation:

$$d = A(m), \tag{1}$$

where A is a forward modeling operator, $m = m(\mathbf{r})$ is a scalar function describing the distribution of the model parameters (density, magnetic susceptibility or electrical conductivity) in some volume V in the Earth, ($m \in M$, where M is a Hilbert space of models with a L_2 norm) and $d = d(\mathbf{r})$ is a geophysical data set ($d \in D$, where D is a Hilbert space of data) formed by observed values of the corresponding geophysical fields (gravity, magnetic or EM).

Inversion aims at determining the model parameters m based on A and some known (observed) data d. This problem is usually ill posed, i.e., the solution can be nonunique and unstable. The conventional way of solving ill-posed inverse problems, according to the regularization theory, is based on the minimization of the Tikhonov parametric functionals:

$$P^{\alpha}(m) = \phi(m) + \alpha s(m) = \min, \tag{2}$$

where $\phi(m)$ is a misfit functional determined as a norm of the difference between observed and predicted (theoretical) data:

$$\varphi(m) = \|Am - d\|_D^2 = (Am - d,\ Am - d)_D. \tag{3}$$

Functional $s(m)$ is a stabilizing functional (stabilizer), and α is a regularization parameter.

The optimal value of α is determined from the misfit condition:

$$\varphi(m_{\alpha}) = \delta_d, \tag{4}$$

where m_{α} is a solution of the minimization problem (2), and δ_d is the noise level of the data.

The stabilizing functional incorporates information about the basic properties of the type of models used in the inversion. The traditional smooth inversion algorithms are based on the minimum norm or maximum smoothness stabilizing functionals (e.g., Occam's inversion). For example, a minimum norm stabilizing functional $s(m)$ is usually selected in the Hilbert metric of model space $M = L_2$ as a norm square of the difference between the current and a priori models:

$$s_{MN}(m) = \|(m - m_{apr})\|_M^2 = (m - m_{apr},\ m - m_{apr})_M = \iiint_V (m - m_{apr})^2\, dv. \tag{5}$$

This stabilizer provides, usually, a relatively smooth image of the inverse model.

This criterion, as applied to the gradient of model parameters $\nabla m_{,}$, brings us to a maximum smoothness stabilizing functional:

$$s_{max\,sm}(m) = \|\nabla m\|_M^2 = (\nabla m,\ \nabla m)_M. \tag{6}$$

This stabilizer produces smooth geological models, which in many practical situations do not describe the real blocky geological structures well.

In order to produce focused images of a target with sharp boundaries, we use a new type of stabilizing functional, the so-called minimum support or minimum gradient support functionals.

In particular, the minimum support functional is a nonquadratic functional of the form (Zhdanov 2002):

$$s_{MS}(m) = \iiint_V \frac{(m - m_{apr})^2}{(m - m_{apr})^2 + e^2} dv, \tag{7}$$

where e is a *focusing* parameter required to avoid the singularity in the last formula for the points where $m = m_{apr}$. The minimum support functional has an important property: it minimizes the total domain (support) with the nonzero departure of the model parameters from a given *a priori* model (Zhdanov 2002). Thus, a dispersed and smoothed distribution of the parameters with all values different from the *a priori* model m_{apr} results in a big penalty function, while a well-focused distribution with a small departure from m_{apr} will have a small penalty function.

Another example of the focusing functional is a minimum gradient support functional determined by the following expression:

$$s_{MGS}(m) = \iiint_V \frac{\nabla m \cdot \nabla m}{\nabla m \cdot \nabla m + e^2} dv. \tag{8}$$

We denote by $\mathrm{spt}\nabla m$ the combined closed subdomains of V where $\nabla m \neq 0$. We call $\mathrm{spt}\nabla m$ a gradient support. Then expression (8) can be modified:

$$s_{MGS}(m) = \iiint_{\mathrm{spt}\nabla m} \left[1 - \frac{e^2}{\nabla m \cdot \nabla m + e^2}\right] dv = \mathrm{spt}\nabla m - e^2 \iiint_{\mathrm{spt}\nabla m} \frac{1}{\nabla m \cdot \nabla m + e^2} dv. \tag{9}$$

From the last expression we can see that:

$$s_{MGS}(m) \to \mathrm{spt}\nabla m, \text{ if } e \to 0. \tag{10}$$

Thus, we can see that $s_{MGS}(m)$ can be treated as a functional proportional (for a small β) to the gradient support. This

functional minimizes the anomalous domains and/or the areas with strong variations of the model parameters, which results in focusing inverse geophysical images (Zhdanov 2002).

MINIMUM SUPPORT INVERSION METHOD

Consider again the inverse geophysical problem (1). We will analyse two important cases of the linear and nonlinear operators A.

Assume first that A is a linear operator. Following the conventional logic of the regularization theory, we reduce the solution of the inverse problem to the minimization of the Tikhonov parametric functional:

$$P^{\alpha}_{MS}(m) = \phi(m) + \alpha s_{MS}(m) =$$

$$(Am - d,\ Am - d)_D + \alpha \iiint_V \frac{(m - m_{apr})^2}{(m - m_{apr})^2 + e^2} dv, \qquad (11)$$

where $s_{MS}(m)$ is a minimum support stabilizing functional.

Let us calculate the first variation of this functional (Zhdanov 2002):

$$\delta P^{\alpha}_{MS}(m) = 2(A\delta m,\ Am - d)_D + 2\alpha e^2 \iiint_V \frac{(m - m_{apr})\delta m}{\left[(m - m_{apr})^2 + e^2\right]^2} dv,$$

or

$$\delta P^{\alpha}_{MS}(m) = 2(\delta m,\ A^{\star}(Am - d))_M + 2\alpha(\delta m,\ B)_M, \qquad (12)$$

where $A^{\star}$ is the adjoint operator of A, and:

$$B = \frac{e^2 (m - m_{apr})}{\left[(m - m_{apr})^2 + e^2\right]^2}.$$

The necessary condition of the functional minimum requires that the first variation of this functional be equal to zero at a minimum. Thus, we have the following equation for m:

$$A^{\star}(Am - d) + \alpha \frac{e^2 t (m - m_{apr})}{\left[(m - m_{apr})^2 + e^2\right]^2} = 0, \quad r \in V. \qquad (13)$$

Equation (13) is the Euler-Lagrange equation for the parametric functional (11) minimization. A solution m_{α} of this equation realizes the minimum of P^{α}_{MS}:

$$P^{\alpha}_{MS}(m_{\alpha}) = \min.$$

However, the direct solution of equation (13) represents a challenging numerical problem. It is more convenient to apply the iterative algorithm of the parametric functional minimization, which we will outline below for a general case of a nonlinear operator.

In the case of the nonlinear forward modelling operator A, the first variation of the parametric functional (11) takes the form:

$$\delta P^{\alpha}_{MS}(m) = 2(\delta m,\ F^{\star}(Am - d))_M + 2\alpha(\delta m,\ B)_M = 2(\delta m,\ F^{\star}(Am - d) + \alpha B)_M < 0 \qquad (14)$$

where F is a Fréchet derivative of A. Following the basic concepts of the steepest descent method, we select:

$$\delta m = -kl(m) \qquad (15)$$

where the gradient direction is equal to:

$$l(m) = F^{\star}(Am - d) + \alpha B. \qquad (16)$$

Note that for the linear forward operator:

$$F = A;$$

therefore the gradient direction is equal to:

$$l(m) = A^{\star}(Am - d) + \alpha B. \qquad (17)$$

On the basis of equations (15) and (16), one can construct steepest descent or conjugate gradient algorithms for inverse problem solutions. In the numerical examples discussed below, we use the conjugate gradient method. The algorithm for the regularized conjugate gradient method, according to Zhdanov (2002), can be summarized as follows:

$$r_n = A(m_n) - d, \quad l^{\alpha}_n = l^{\alpha}(m_n) = F^{\star}_{m_n}(Am_n - d) + \alpha B_n \quad (a)$$

where $B_n = e^2(m_n - m_{apr})/\left[(m_n - m_{apr})^2 + e^2\right]^2$

$$\beta^{\alpha}_n = \|l^{\alpha}_n\|^2 / \|l^{\alpha}_{n-1}\|^2, \quad \tilde{l}^{\alpha}_n = l^{\alpha}_n + \beta^{\alpha}_n \tilde{l}^{\alpha}_{n-1}, \quad \tilde{l}^{\alpha}_0 = l^{\alpha}_0, \quad (b) \qquad (18)$$

$$\tilde{k}^{\alpha}_n = (\tilde{l}^{\alpha}_n,\ l^{\alpha}_n) / \left\{\|F_{m_n}\tilde{l}^{\alpha}_n\|^2 + \alpha \|\tilde{l}^{\alpha}_n\|^2\right\}, \quad (c)$$

$$m_{n+1} = m_n - \tilde{k}^{\alpha}_n \tilde{l}^{\alpha}_n. \quad (d)$$

The iterative process (18) is terminated when the misfit reaches the required level:

$$\varphi(m_{n+1}) = \delta_d. \qquad (19)$$

Note that the regularized conjugate gradient method (18) can be applied to the solution of both linear and nonlinear geophysical inverse problems.

MINIMUM GRADIENT SUPPORT INVERSION METHOD

Now we introduce the Tikhonov parametric functional with the minimum gradient support stabilizer:

$$P^{\alpha}_{MGS}(m) = \varphi(m) + \alpha s_{MGS}(m)$$

$$= (Am-d,\ Am-d)_D + \alpha \iiint_V \frac{\nabla m \cdot \nabla m}{\nabla m \cdot \nabla m + e^2} dv. \quad (20)$$

Let us take a variation of the last formula, assuming first that A is a linear operator:

$$\delta P^{\alpha}_{MGS}(m) = 2(A\delta m,\ Am-d)_D + \alpha \delta s_{MGS}(m). \quad (21)$$

Calculating the first variation of the minimum gradient support functional, we find:

$$\delta s_{MGS}(m) = \delta \iiint_V \frac{\nabla m \cdot \nabla m}{\nabla m \cdot \nabla m + e^2} dv$$

$$= 2 \iiint_V (\mathbf{C} \cdot \nabla \delta m)_M \, dv, \quad (22)$$

where

$$\mathbf{C} = b^2 \nabla m \quad (23)$$

and

$$b^2 = \frac{e^2}{(\nabla m \cdot \nabla m + e^2)^2}.$$

Using the identity:

$$\nabla \cdot (\mathbf{C}\delta m) = (\nabla \cdot \mathbf{C})\delta m + \mathbf{C} \cdot \nabla \delta m,$$

we can integrate the integral (22) by parts:

$$\iiint_V (\mathbf{C} \cdot \nabla \delta m)\, dv = -\iiint_V (\nabla \cdot \mathbf{C})\delta m dv$$

$$+ \iiint_V \nabla \cdot (\mathbf{C}\delta m)\, dv = -\iiint_V (\nabla \cdot \mathbf{C})\delta m dv$$

$$+ \iint_{\partial V} \mathbf{C}\delta m \cdot \mathbf{n} ds,$$

where we have applied the Gauss theorem, and $\mathbf{n}$ is a unit vector of the normal directed outward from the domain V.

We assume homogeneous Neumann (i.e., no flux) boundary conditions:

$$\iint_{\partial V} \mathbf{C}\delta m \cdot \mathbf{n} ds = \iint_{\partial V} \delta m b^2 \nabla m \cdot \mathbf{n} ds = 0.$$

The last condition can be reformulated as:

$$\nabla m \cdot \mathbf{n} = \frac{\partial m}{\partial n} = 0, \quad r \in \partial V, \quad (24)$$

where $\partial m/\partial n$ is a directional derivative in the direction of vector $\mathbf{n}$. Therefore we have:

$$\delta s_{MGS}(m) = 2 \iiint_V (\mathbf{C} \cdot \nabla \delta m)\, dv = -2 \iiint_V (\nabla \cdot \mathbf{C})\delta m dv$$

$$= -2(\delta m, (\nabla \cdot \mathbf{C}))_M. \quad (25)$$

Substituting (25) into (21), we obtain:

$$\delta P^{\alpha}_{MGS}(m) = 2(A\delta m,\ Am-d)_D + 2\alpha \iiint_V \mathbf{C} \cdot \nabla \delta m dv$$

$$= 2(\delta m,\ A^*(Am-d))_M - \alpha \iiint_V (\nabla \cdot \mathbf{C})\delta m dv$$

$$= (\delta m,\ [A^*(Am-d) - \alpha(\nabla \cdot \mathbf{C})])_M.$$

The necessary condition of the functional minimum requires that the first variation of this functional be equal to zero at a minimum. Thus we have the following Euler-Lagrange equation for m:

$$A^*(Am-d) - \alpha(\nabla \cdot b^2 \nabla m) = 0, \quad r \in V, \quad (26)$$

and the boundary condition:

$$\frac{\partial m}{\partial n} = 0. \quad (27)$$

A solution m_α of these equations realizes the minimum of the parametric functional $P^{\alpha}_{MGS}(m_\alpha) = \min$.

Note that the direct solution of the Euler-Lagrange equation (26) is very complicated. A less computationally expansive approach is based on the iterative gradient type inversion, which could be applied to the inverse problems with both linear and nonlinear forward modelling operators. For example, in the case of nonlinear operator A, the expression for the first variation of the parametric functional (20) takes the form:

$$\delta P^{\alpha}_{MGS}(m) = 2(\delta m,\ [F^*(Am-d) - \alpha(\nabla \cdot \mathbf{C})])_M. \quad (28)$$

Following the basic concepts of the steepest descent method, we select:

$$\delta m = -kl(m),$$

where $l(m)$ is a gradient direction:

$$l(m) = F^*(Am-d) - \alpha(\nabla \cdot \mathbf{C}).$$

Knowing the gradient direction, we can apply the steepest descent or conjugate gradient method to find the solution of the inverse problem. The algorithm for the regularized conjugate gradient method (18) can be modified as follows:

$$r_n = A(m_n) - d,\ l^{\alpha}_n = l^{\alpha}(m_n) = F_{m_n}{}^*(Am_n - d) + \alpha(\nabla \cdot \mathbf{C}_n), \quad (a)$$

where $\mathbf{C}_n = e^2 \nabla m_n / (\nabla m_n \cdot \nabla m_n + e^2)^2$,

$$\beta^{\alpha}_n = \|l^{\alpha}_n\|^2 / \|l^{\alpha}_{n-1}\|^2, \quad \tilde{l}^{\alpha}_n = l^{\alpha}_n + \beta^{\alpha}_n \tilde{l}^{\alpha}_{n-1}, \ \tilde{l}^{\alpha}_0 = l^{\alpha}_0, \quad (b)$$

$$\tilde{k}^{\alpha}_n = (\tilde{l}^{\alpha}_n,\ l^{\alpha}_n) / \left\{ \|F_{m_n} \tilde{l}^{\alpha}_n\|^2 + \alpha \|\tilde{l}^{\alpha}_n\|^2 \right\}, \quad (c)$$

$$m_{n+1} = m_n - \tilde{k}^{\alpha}_n \tilde{l}^{\alpha}_n. \quad (d) \quad (29)$$

The iterative process (29) is terminated based on condition (19).

The basic principles used for determining the regularization parameter α are as follows. Consider for example the progression of numbers:

$$\alpha_k = \alpha_1 q^{k-1}; \quad k = 1, 2, 3 \ldots; q > 0. \tag{30}$$

The first iteration of the steepest descent of the conjugate gradient method is run usually with $\alpha_0 = 0$. The initial value of the regularization parameter, α_1, is determined after the first iteration, $\mathbf{m}_1$, as a ratio:

$$\alpha_1 = \frac{\| A(m_1) - d \|^2}{\| m_1 - m_{apr} \|^2}.$$

In this way we have an approximate balance between the misfit and stabilizing functionals. Then we reduce α_n according to formula (30) on each subsequent iteration and continuously iterate until the misfit condition (4) is reached. This approach to the optimal regularization parameter selection is called adaptive regularization (Zhdanov 2002).

In the following sections I will illustrate the principles of focusing inversion using the examples of airborne gravity gradiometer data and land and marine magnetotelluric data.

FOCUSING INVERSION OF GRAVITY GRADIOMETER DATA

Airborne gravity gradiometer data

Recent technological developments made it possible to accurately measure all the independent tensor components of the gravity gradient field from an airborne platform. Previous research has demonstrated that the use of airborne gravity gradient data can significantly improve inversion results and increase the effectiveness of the gravity method in mineral exploration (Zhdanov, Ellis and Mukherje 2004). The technology that enables such rapid and accurate data acquisition motivates the research to further develop methods for processing and interpreting gradiometer data. Moreover, these advancements continue to stimulate a growing interest in the application of gravity gradient data in geophysical exploration.

Here I provide a brief mathematical description of the gravity tensor components (after Zhdanov *et al.* 2004), which are measured by airborne gravity gradiometers. First, we know that the gravity field, $\mathbf{g}$, must satisfy the following equations (Zhdanov 1988):

$$\nabla \cdot \mathbf{g} = -4\pi\gamma\rho, \; \nabla \times \mathbf{g} = 0, \tag{31}$$

where γ is the universal gravitational constant and ρ is the anomalous density distribution within a domain D.

The solution of these equations is given by the formula:

$$\mathbf{g}(\mathbf{r}) = \gamma \iiint_D \rho(\mathbf{r}') \frac{\mathbf{r}' - \mathbf{r}}{|\mathbf{r}' - \mathbf{r}|^3} \, dv', \tag{32}$$

where integration is conducted over the variable $\mathbf{r}'$. The gravity field can be expressed by the gravity potential $U(\mathbf{r})$ as

$$\mathbf{g}(\mathbf{r}) = \nabla U(\mathbf{r}),$$

where:

$$U(\mathbf{r}) = \gamma \iiint_D \frac{\rho(\mathbf{r}')}{|\mathbf{r}' - \mathbf{r}|^3} \, dv'. \tag{33}$$

The second spatial derivatives of the gravity potential $U(\mathbf{r})$:

$$g_{\alpha\beta}(\mathbf{r}) = \frac{\partial^2}{\partial\alpha\partial\beta} U(\mathbf{r}), \quad \alpha, \beta = x, y, z, \tag{34}$$

form a symmetric gravity tensor:

$$\hat{\mathbf{g}} = \begin{bmatrix} g_{xx} & g_{xy} & g_{xz} \\ g_{yx} & g_{yy} & g_{yz} \\ g_{zx} & g_{zy} & g_{zz} \end{bmatrix},$$

where:

$$g_{\alpha\beta} = \frac{\partial g_\alpha}{\partial\beta}, \quad \alpha, \beta = x, y, z. \tag{35}$$

The expressions for the gravity tensor components can be calculated based on formulae (34) and (33):

$$g_{\alpha\beta}(\mathbf{r}) = \gamma \iiint_D \frac{\rho(\mathbf{r}')}{|\mathbf{r}' - \mathbf{r}|^3} K_{\alpha\beta}(\mathbf{r}' - \mathbf{r}) \, dv', \tag{36}$$

where kernels $K_{\alpha\beta}$ are equal to:

$$K_{\alpha\beta}(\mathbf{r}' - \mathbf{r}) = \begin{cases} 3\frac{(\alpha - \alpha')(\beta - \beta')}{|\mathbf{r}' - \mathbf{r}|^2}, & \alpha \neq \beta \\ 3\frac{(\alpha - \alpha')^2}{|\mathbf{r}' - \mathbf{r}|^2} - 1, & \alpha = \beta \end{cases}, \quad \alpha, \beta = x, y, z. \tag{37}$$

Using formulae (36) and (37), derived above, we write the following expressions for the gravity tensor components in discretized form, considering each cell as a point mass:

$$g_{xx}(\mathbf{r}) = \gamma \sum_D \rho(\mathbf{r}') \frac{1}{|\mathbf{r}' - \mathbf{r}|^3} \left(3\frac{(x' - x)^2}{|\mathbf{r}' - \mathbf{r}|^2} - 1 \right) \Delta x' \Delta y' \Delta z'. \tag{38}$$

$$g_{xy}(\mathbf{r}) = 3\gamma \sum_D \rho(\mathbf{r}') \left(\frac{(x' - x)(y' - y)}{|\mathbf{r}' - \mathbf{r}|^5} - 1 \right) \Delta x' \Delta y' \Delta z'. \tag{39}$$

$$g_{xz}(\mathbf{r}) = 3\gamma \sum_D \rho(\mathbf{r}') \left(\frac{(x' - x)(z' - z)}{|\mathbf{r}' - \mathbf{r}|^5} - 1 \right) \Delta x' \Delta y' \Delta z'. \tag{40}$$

$$g_{zz}(\mathbf{r}) = \gamma \sum_D \rho(\mathbf{r}') \frac{1}{|\mathbf{r}' - \mathbf{r}|^3} \left(3\frac{(z' - z)^2}{|\mathbf{r}' - \mathbf{r}|^2} - 1 \right) \Delta x' \Delta y' \Delta z'. \tag{41}$$

The point-mass approximation dramatically speeds up the processing time while yielding very accurate results. In a paper by Jessop and Zhdanov (2005a), the accuracy of this approximation was quantitatively examined by comparing it to the exact prism body method given by Okabe (1979). It was demonstrated in the cited paper that, when the depth to the centre of the cell exceeds twice the dimension of the cell, the error level quickly falls below one-half of a percent. At the same time the point-mass approximation method is up to 10 times faster, depending on the ratio of the observation points to cells; furthermore, the point-mass approximation requires only one-tenth the amount of memory in comparison with the exact prismatic body method. This is why in our computer algorithm we use formulae (38)–(41) for forward modelling calculations of the tensor gravity field.

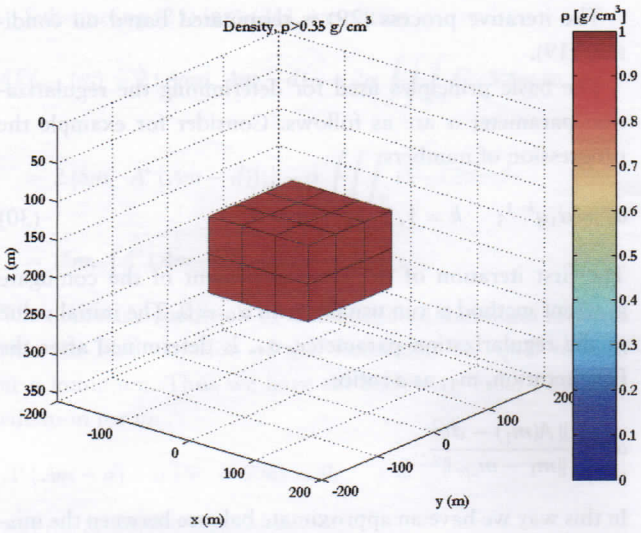

Figure 1 Model 1: a rectangular body with an anomalous density of 1 g/cm^3.

Inversion of airborne gravity data in areas with rough topography

In an area with little topographical variation, the observation data can usually be acquired at a uniform altitude; in this situation, we can generally assume that the data lie in a horizontal plane and that a regular 3D mesh is sufficient to model the flat terrain.

Many airborne survey areas, however, cover rough terrain, and the flight surface is necessarily uneven. In such cases, a rectangular 3D mesh is inadequate for modeling the subsurface. A new approach has been designed by Jessop and Zhdanov (2005b) to handle variations in the topography as well as those in the flight surface. To set up the modelling domain, we first define subsurface cell locations in a regular 3D mesh and then by incorporating topographical data we can adjust each column of cells relative to the interpolated elevation directly over each column. This allows for areas with rough topography to be modelled without having to use a rectangular domain that can intersect the space of the observed data. This method also ensures a more efficient use of computer memory by not creating useless cells that lie above the topography.

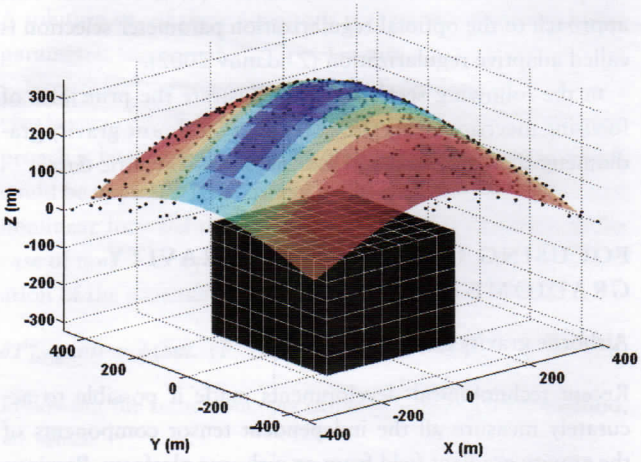

Figure 2 Modelling domain and arbitrary observation surface with a texture map of the g_{yy} data. A colour scale of the texture map is the same as in Fig. 8. Observation points are posted as black dots.

Model 1: Single body

For our first model study, we attempt to recover a rectangular body from data computed on an arbitrary surface. The rectangular prism body has dimensions 150 × 150 × 100 metres, has an anomalous density of 1.0 g/cm^3, and is centered 125 metres below the subsurface (see Fig. 1). We computed the synthetic data for g_{yy} on the arbitrary observation surface shown in Fig. 2, where elevations range from about 20 to 350 metres. In the modelling domain, we use a regular mesh with 378 cells.

Figures 3 and 4 present the smooth inversion results, obtained with the minimum norm stabilizer. In the 3D inversion image in Fig. 3 only cells with a density that exceeds 0.07 g/cm^3 are plotted. Figure 4 shows a vertical section of the inverted density. One can see that the smooth inverse image is very diffuse and provides significantly underestimated values of the density.

Figure 5 shows our focused inversion result, where cells that exceed 0.35 g/cm^3 are plotted. Figure 6 presents the vertical

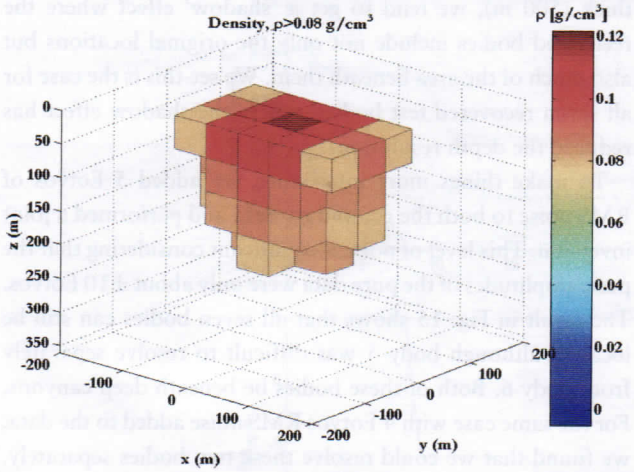

Figure 3 The results of smooth g_{yy} inversion for Model 1, obtained with the minimum norm stabilizer. Only cells with a density that exceeds 0.07 g/cm^3 are plotted.

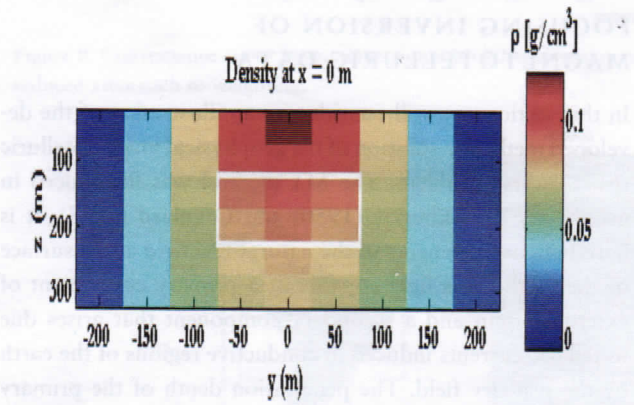

Figure 4 A vertical section of the inverted density obtained by a smooth inversion.

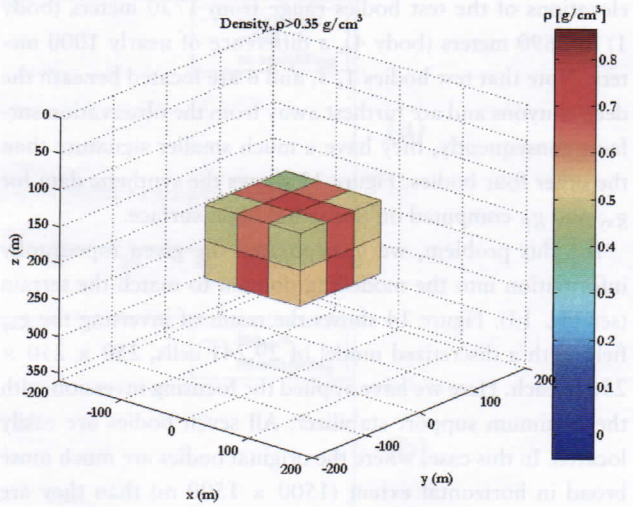

Figure 5 Result of focusing g_{yy} inversion for Model 1 without Gaussian noise.

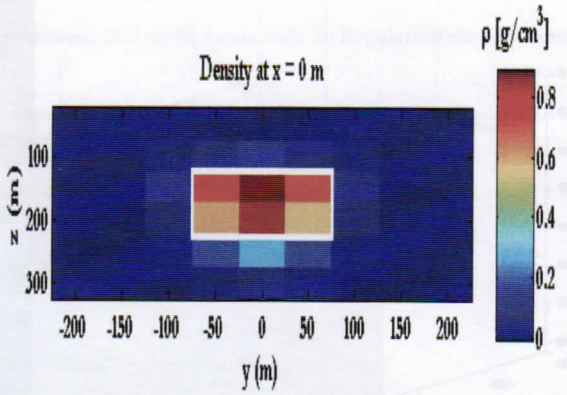

Figure 6 A vertical section of the inverted density obtained by a focusing inversion.

section of the inverted density. Clearly, the body is recovered very well with anomalous densities up to 0.85 g/cm^3. If we add 10% random noise to the data, the body is still recovered exceptionally well (see Fig. 7). The observed and predicted data for this case are shown in Fig. 8. Figure 9 presents the convergence plots for parametric and misfit functionals and for a regularization parameter. We can see that the algorithm quickly achieves a misfit level of around 0.01. This corresponds to a predicted norm of errors (or the square root of misfit) equal to 10%, as expected.

Model 2: Mocha synthetic gravity tensor data

Our second model was provided by BHP Billiton along with the synthetic data for two gravity gradiometer components, g_{xy} and g_{Δ}, both of which are directly measured by BHP's Falcon® airborne gradiometer system. The component g_{Δ} is a combination of two other tensor components and is given by:

$$g_{\Delta} = \frac{g_{xx} - g_{yy}}{2}.$$

The data were computed for seven test bodies on a real flight surface covering more than 200 square kilometres over the Mocha porphyry copper deposit in northern Chile (see Fig. 10). The region is characterized by deep canyons and extremely steep topography rising generally to the east. The test bodies have an anomalous density of 0.2 g/cm^3 and are 1500 × 1500 × 500 meters in size. Figure 11 shows the location of each body numbered 1 to 7 on the topography map. Each body is centered 350 metres below the topography at the corresponding easting and northing location. The

elevations of the test bodies range from 1730 meters (body 1) to 2690 meters (body 4), a difference of nearly 1000 meters. Note that test bodies 1, 5, and 6 are located beneath the deep canyons and are furthest away from the observation surface; consequently, they have a much smaller signature than the other four bodies. Figure 12 shows the synthetic data for g_{xy} and g_{Δ} computed on the actual flight surface.

For this problem, we incorporated the given topography information into the modelling domain to match the terrain (see Fig. 13). Figure 14 shows the result of inverting the g_{xy} field with a discretized model of 29,241 cells, 250 × 250 × 250 m each. Here we have applied the focusing inversion with the minimum support stabilizer. All seven bodies are easily located. In this case, where the original bodies are much more broad in horizontal extent (1500 × 1500 m) than they are thick (500 m), we tend to get a 'shadow' effect where the recovered bodies include not only the original locations but also much of the area beneath them. We see this is the case for all seven recovered test bodies, where the shadow effect has reduced the depth resolution.

To make things more interesting, we added 5 Eotvos of RMS noise to both the g_{xy} and g_{Δ} data and performed a joint inversion. This level of noise is significant considering that the peak amplitudes of the pure data were only about ±10 Eotvos. The result in Fig. 15 shows that all seven bodies can still be located, although body 5 was difficult to resolve separately from body 6. Both of these bodies lie beneath deep canyons. For the same case with 4 Eotvos RMS noise added to the data, we found that we could resolve these two bodies separately. The observed and predicted fields are given for g_{xy} and g_{Δ} in Figs 16 and 17, respectively.

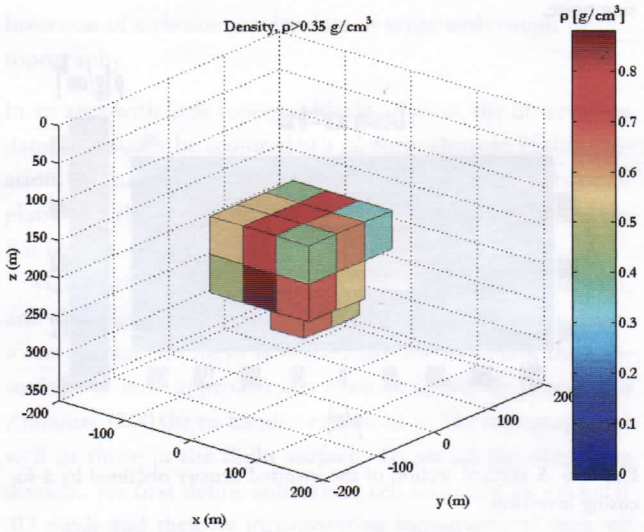

Figure 7 Result of focusing g_{yy} inversion for Model 1 with 10% Gaussian noise added.

FOCUSING INVERSION OF MAGNETOTELLURIC DATA

In this section, we will consider, as an illustration of the developed method, a solution of the geophysical magnetotelluric (MT) inverse problem. The MT method was introduced in geophysics by Tikhonov (1950) and Cagniard (1953). It is based on measurements of the natural EM field at the surface of the earth. This field consists of a primary component of external origin and a secondary component that arises due to telluric currents induced in conductive regions of the earth by the primary field. The penetration depth of the primary field, and therefore of the telluric currents, increases with period. The interpretation of magnetotelluric data is based on the calculation of the transfer functions between the horizontal components of the electric and magnetic fields, which

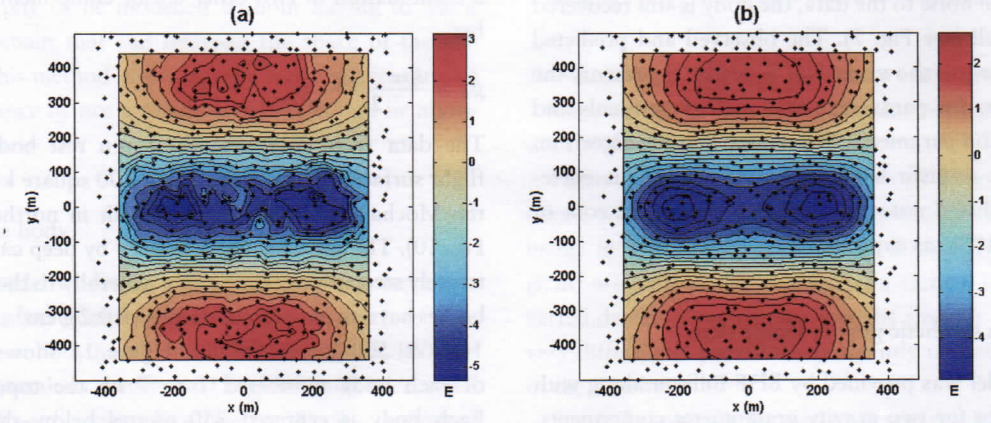

Figure 8 Synthetic g_{yy} data. for Model 1: (a) observed data with 10% noise; (b) predicted data.

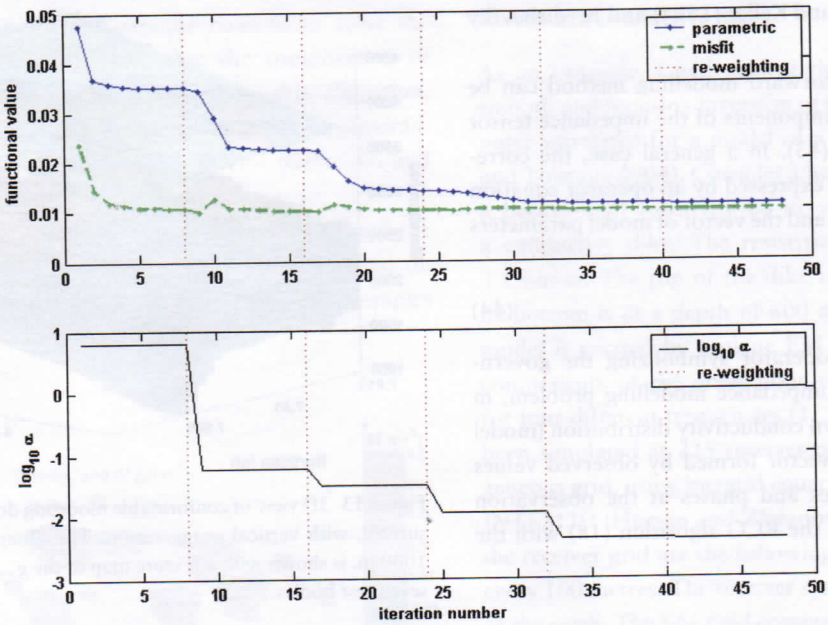

Figure 9 Convergence curve for g_{yy} inversion with 10% Gaussian noise. a) Parametric and misfit functionals. b) Regularization parameter α is reduced after each re-weighting.

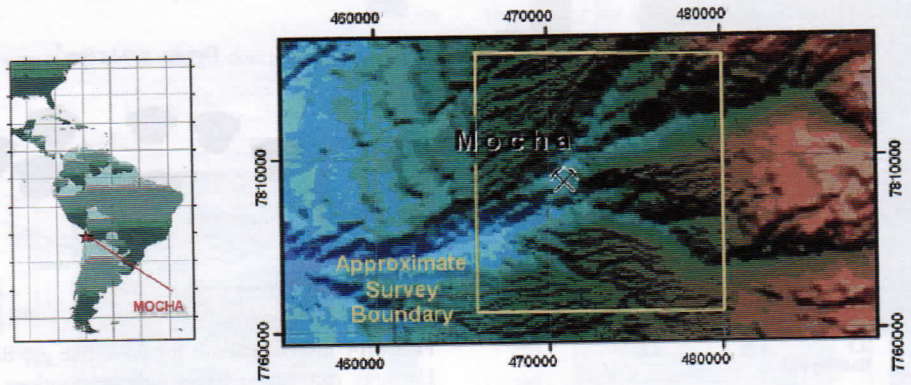

Figure 10 Location of Mocha porphyry copper deposit and approximate survey boundary in northern Chile. The numbers on the x and y axes are UTM coordinates.

form the so-called impedance tensor $\widehat{\mathbf{Z}}$ (Zhdanov and Keller 1994). The components of the impedance tensor depend primarily on the subsurface resistivity distribution over the penetration depth. Impedance measurements as a function of period can therefore be inverted for a resistivity model of the earth.

Following the traditional approach used in practical MT observations, we can calculate the apparent resistivities, ρ, and phases, ϕ, based on two off-diagonal elements of the MT tensor, Z_{xy} and Z_{yx}, at each observation point,

$$\rho_{xy} = \frac{1}{\omega\mu_0}|Z_{xy}|^2, \quad \rho_{yx} = \frac{1}{\omega\mu_0}|Z_{yx}|^2, \tag{42}$$

$$\phi_{xy} = \tan^{-1}\frac{ImZ_{xy}}{ReZ_{xy}}, \quad \phi_{yx} = \tan^{-1}\frac{ImZ_{yx}}{ReZ_{yx}}. \tag{43}$$

where the quantities ρ_{xy} and ϕ_{xy} are assigned to the nominal transverse magnetic (TM) mode, whereas ρ_{yx} and ϕ_{yx} are assigned to the nominal transverse electric (TE) mode. Note that, in inversion algorithm we actually use the logarithm of apparent resistivity and phase in radians.

The solution of the inverse problem requires numerical modelling of the apparent resistivities and phases in each step of the iteration process. The components of the impedance tensor are determined from the horizontal components of the electric and magnetic fields in every observation point. The corresponding technique of solving this problem is outlined,

for example, in Zhdanov and Keller (1994) and Berdichevsky and Dmitriev (2002).

The integral equation forward modelling method can be used for computing the components of the impedance tensor components in (42) and (43). In a general case, the corresponding formulae can be expressed by an operator equation including the data vector **d** and the vector of model parameters **m** as

$$\mathbf{d} = \mathbf{A}(\mathbf{m}), \tag{44}$$

where **A** is the forward operator symbolizing the governing equations of the MT impedance modelling problem, **m** is the vector of the unknown conductivity distribution (model parameters) and **d** is the vector formed by observed values of the apparent resistivities and phases at the observation points. We can now apply the RCG algorithm (18) with the

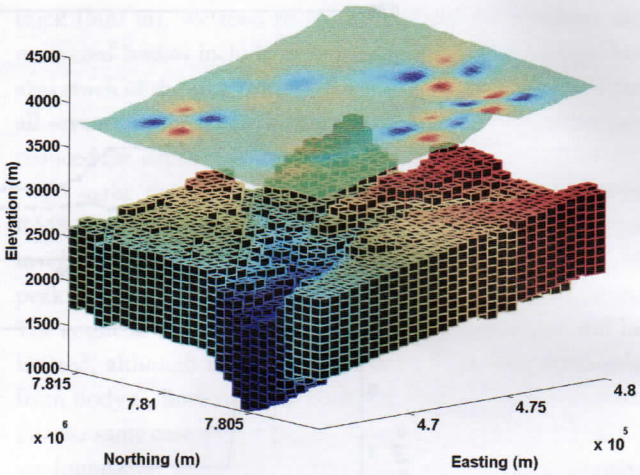

Figure 13 3D view of conformable modeling domain and observation surface, with vertical exaggeration. The observation surface, raised 1000 m, is shown with a texture map of the g_{xy} data produced by the seven test bodies.

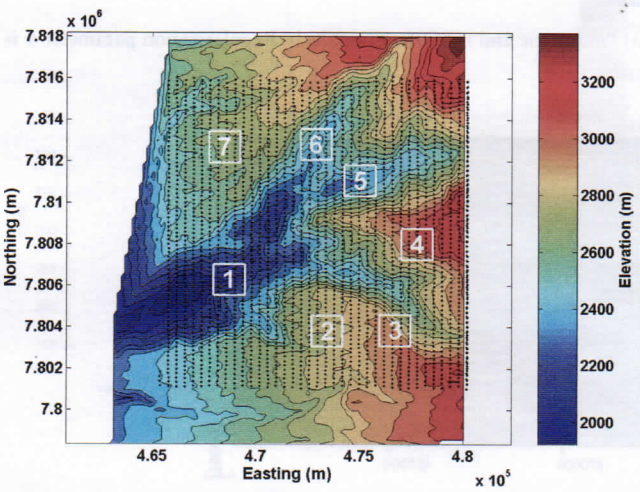

Figure 11 Map view of the Mocha survey area topography with posted observation coordinates. Locations of the seven test bodies are shown. Each body is centered 350 metres below the surface.

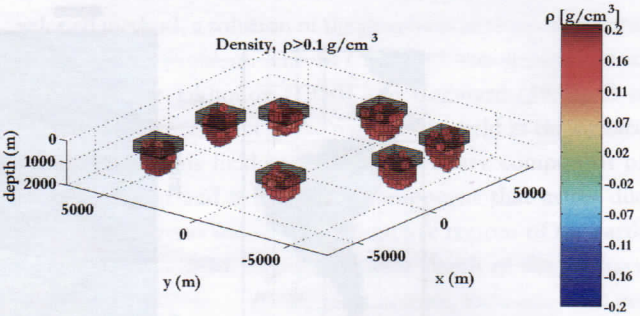

Figure 14 Inversion result for noise-free g_{xy} data for seven bodies. Flat gray rectangular boxes indicate positions of the original bodies. The *x*-*y* coordinate origin corresponds to UTM coordinates 472, 775 m easting, 7,808,450 m northing.

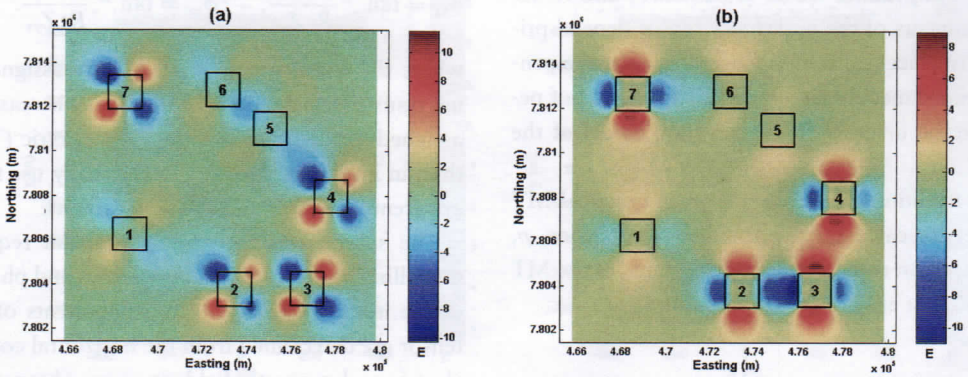

Figure 12 Synthetic data generated by BHP Billiton for seven test bodies. (a) g_{xy} component; (b) g_{Δ} component.

minimum support nonlinear parameterization to solve the MT inverse problem (44). Note that the computation of the Fréchet derivative matrix, required by this algorithm, can be made on the basis of quasi-analytical approximation with the variable background – QAVB (Gribenko and Zhdanov 2007).

The 3D MT inversion algorithm described above and the corresponding computer code has been carefully tested on synthetic models. I present below some numerical examples of the MT data inversion with this method.

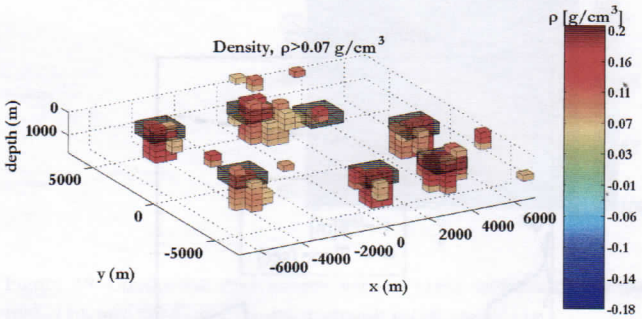

Figure 15 Joint inversion result of g_{xy} and g_{Δ} components, each with 5 E RMS noise.

Model 3: a conductive dike

As an example, I will present the results obtained using a smooth and focusing inversion of the synthetic MT data computer simulated for a model of a conductive dike (Zhdanov and Tolstaya 2004). Consider a homogeneous half-space with a background resistivity of $\rho_b = 100$ Ohm-m, containing a conductive dike. The resistivity of the inhomogeneity is 3 Ohm-m. The top of the dike is at a depth of 200 m and its bottom is at a depth of 600 m beneath the surface. This model is excited by a plane EM wave source. The x and y components of the anomalous magnetic and electric fields for four different frequencies (1, 10, 100 and 1000 Hz) have been simulated at 225 receiver points arranged on a homogeneous grid, using integral equation forward modelling code INTEM3D (Hursán and Zhdanov 2002). The coordinates of the receiver grid are the following: x and y from -700 to 700 every 100 metres. The receiver system is located at the surface of the earth. The EM field components were recalculated into MT apparent resistivity and phase, using the standard formulae (Berdichevsky and Dmitriev 2002). The area of inversion is covered by a homogeneous mesh consisting of 16 × 25 × 8 cubic cells surrounding the anomalous structure to be inverted. Each cell has a dimension of 100 m in the x, y and z directions.

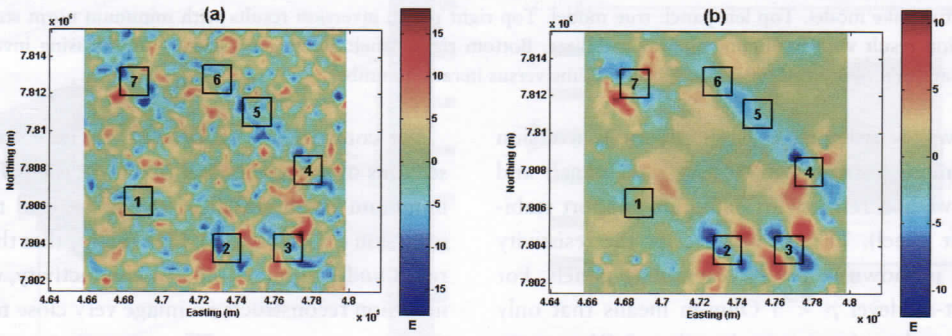

Figure 16 Synthetic g_{xy} component. a) Observed field with 5 E RMS noise; b) Predicted field.

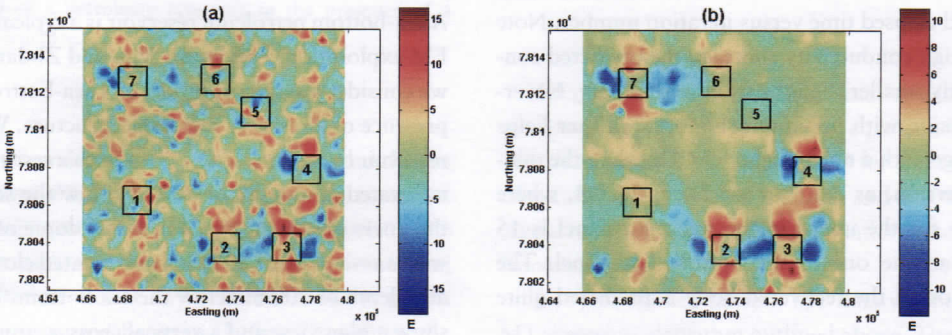

Figure 17 Synthetic g_{Δ} component. a) Observed field with 5 E RMS noise; b) Predicted field.

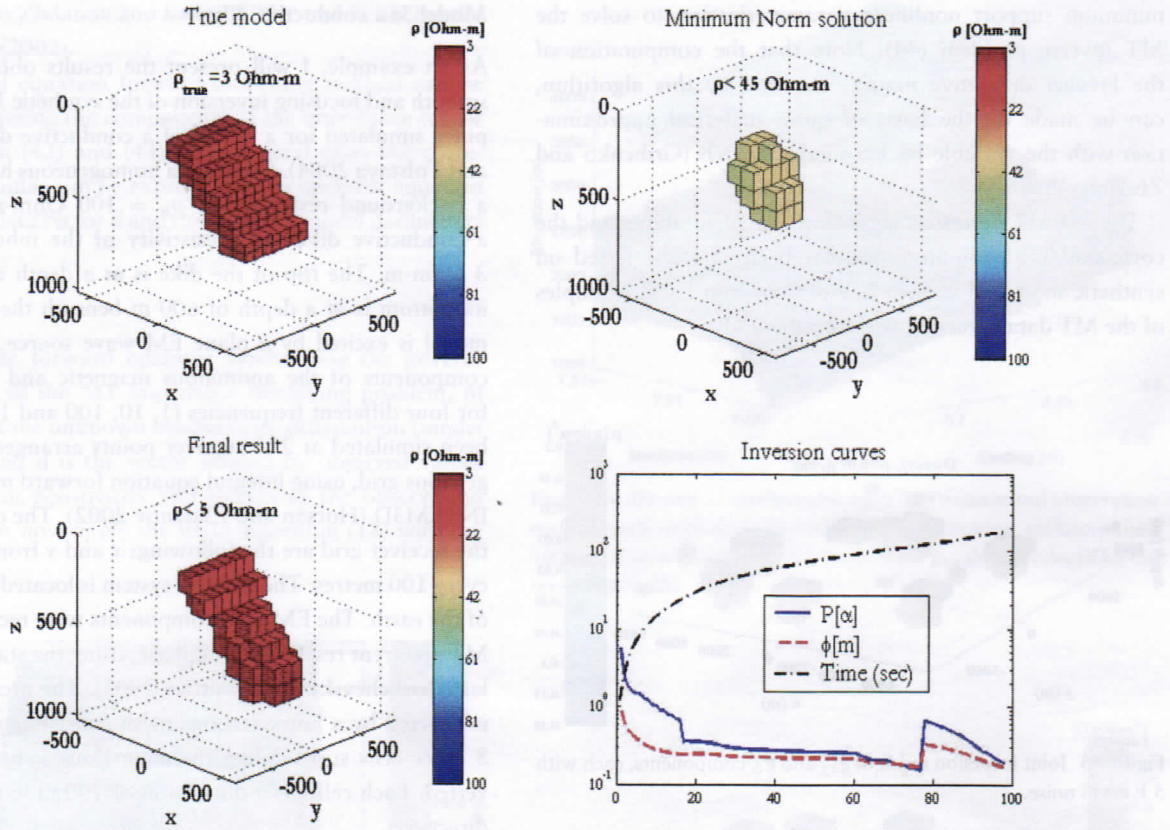

Figure 18 Conductive dike model. Top left panel: true model. Top right panel: inversion results with minimum norm stabilizer. Bottom left panel: final inversion result with minimum support stabilizer. Bottom right panel: convergence curves for focusing inversion – parametric functional, $P[\alpha]$, stabilizer, $S[m]$, misfit, $\phi[m]$ and elapsed time versus iteration number.

Figure 18 shows the true model (top left panel), inversion result with minimum norm stabilizer (top right panel) and final focusing inversion result with minimum support stabilizer (bottom left panel). The cut-off level of the resistivity for these images is shown in the corresponding panels. For example, the cut-off level $\rho < 3$ Ohm-m means that only the cells with the value of resistivity less than 3 Ohm-m are displayed. The bottom right panel of Fig. 18 presents the inversion curves, parametric functional, $P[\alpha]$, stabilizer, $S[m]$, misfit, ϕ $[m]$, and elapsed time versus iteration number. Note that due to the high conductivity contrast, the predicted conductivity is slightly smaller than the true conductivity. Nevertheless, the inversion with minimum support stabilizer helps to obtain an image with a much higher contrast than the minimum norm inversion, as one can see from Fig. 18, where the cut-off value for the image in the top right panel is 15 times greater than the one in the bottom left panel. The shape and position of the recovered body is predicted quite well.

For comparison, we present in Fig. 19 the vertical cross-sections of the true model (panel a), the inversion result with minimum norm stabilizer (panel b), and the final focusing inversion result (panel c). One can see that the minimum norm result underestimates the true conductivity, while the focusing inversion reconstructs an image very close to the true model.

Model 4: a sea-bottom petroleum reservoir

A sea-bottom petroleum reservoir is a typical target for marine EM exploration. Following Wan and Zhdanov (2003, 2004), we consider a synthetic model of a sea-bottom reservoir in the presence of a resistive salt dome structure. We approximate a reservoir by a thin resistive body with a resistivity of 100 Ohm-m located at a depth of 500 m below the sea bottom, with a thickness of 100 m (Fig. 20). A salt dome of a complex shape with a resistivity of 30 Ohm-m is located close to the reservoir, at a depth of 300 m below the sea bottom. Figures 21 and 22 show a plan view and a vertical cross section of Model 4. The

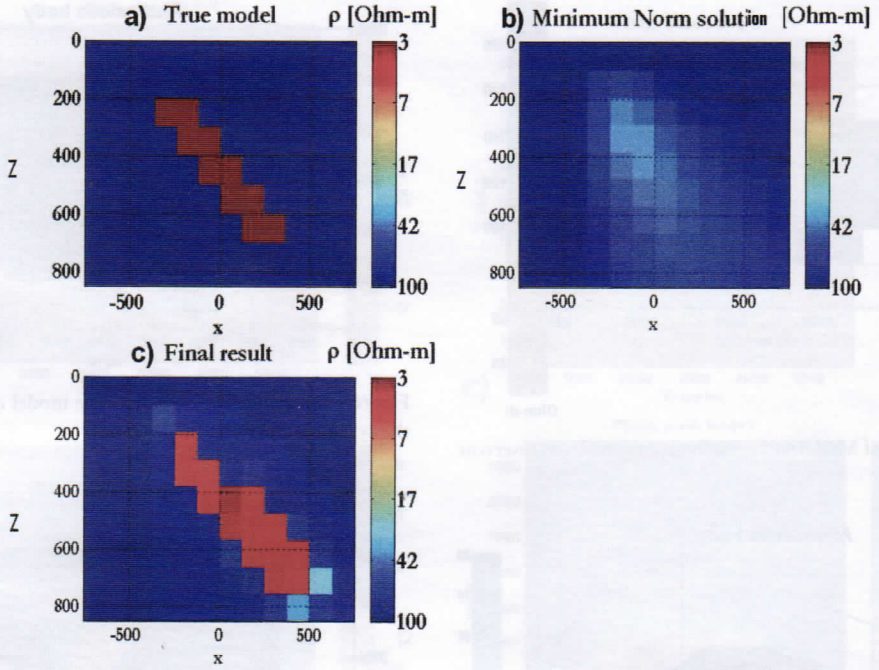

Figure 19 Conductive dike model: vertical cross sections of the true model (panel a), the inversion result with minimum norm stabilizer (panel b), and the final focusing inversion result (panel c).

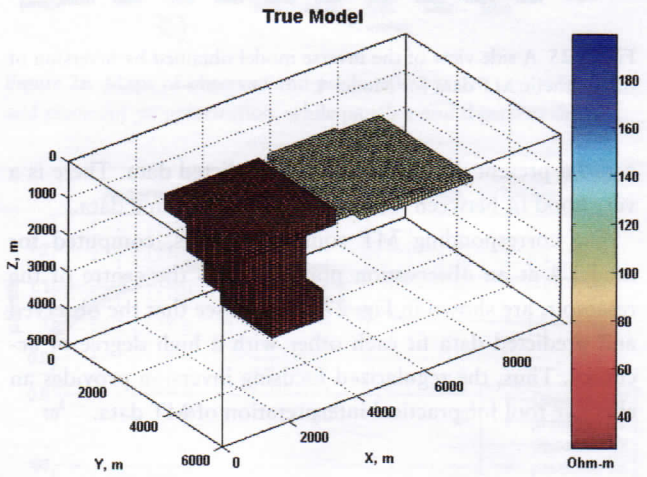

Figure 20 Model 4 of a petroleum reservoir in the presence of a resistive salt dome structure.

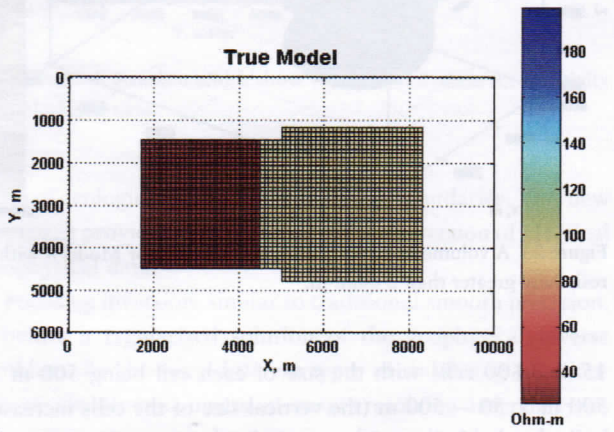

Figure 21 A plan view of Model 4 of a sea-bottom petroleum reservoir and a salt dome.

depth of the sea bottom is 500 m from the surface, and the sea water resistivity is equal to 0.25 Ohm-m. This model is excited by a vertically propagated plane electromagnetic wave. The magnetotelluric stations are located at the sea bottom along 12 lines parallel to the axis x, with 20 observation points in each line. The separation between the lines is 500 m, the observation step along the line is 500 m as well.

The synthetic sea-bottom MT data for Model 4 were generated using the INTEM3D integral equation forward modeling code (Hursán and Zhdanov, 2002) for eight different frequencies: 1, 0.3, 0.1, 0.03, 0.01, 0.003, and 0.001 Hz, and the data (apparent resistivity) have been contaminated by 3% random Gaussian noise.

The synthetic sea-bottom MT data were inverted using the MT inversion algorithm outlined above. The area of inversion is located under the sea bottom. It is divided into 20 × 12 ×

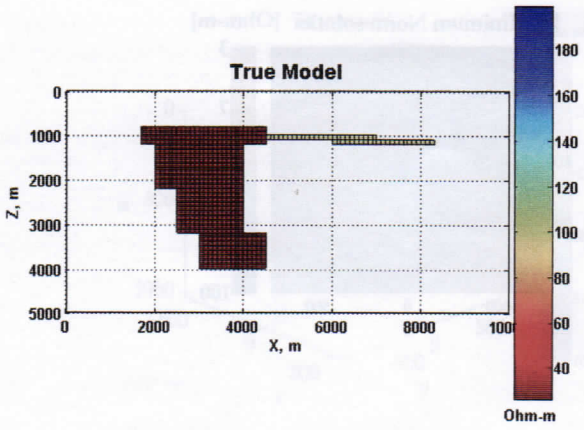

Figure 22 A side view of Model 4 of a sea-bottom petroleum reservoir and a salt dome.

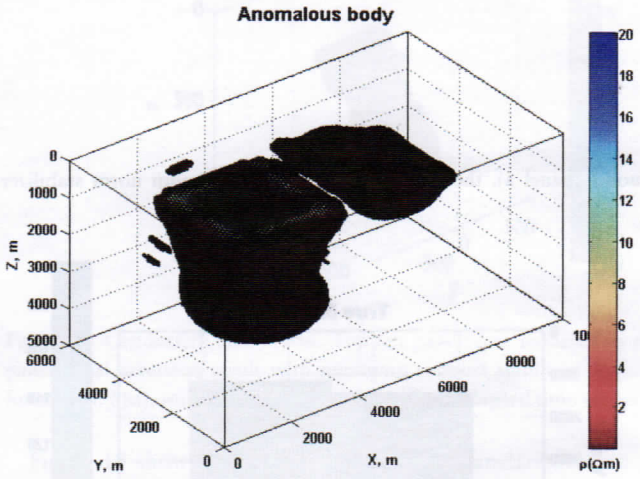

Figure 23 A volume image of the inversion result for Model 4 with a resistivity greater than 2 Ohm-m.

15 = 3,600 cells with the size of each cell being 500 m × 500 m × 50 – 500 m (the vertical size of the cells increases with the depth from 50 m to 500 m). Figure 23 shows the volume image of the inversion result with a resistivity greater than 2 Ohm-m. One can clearly see both the reservoir and a salt dome in this image. Figures 24 and 25 present plan and side views, respectively, of the inverse model obtained by the inversion of the synthetic MT data for model 4.

We should note that the corresponding smooth inversion was not able to resolve the salt dome and the reservoir separately and resulted in one diffusive resistive zone covering both targets.

We present in Fig. 26 the maps of the Z_{yx} apparent resistivity and phase for the frequency 0.03 Hz. The maps of synthetic 'observed' MT data are shown in panels a and b, while panels

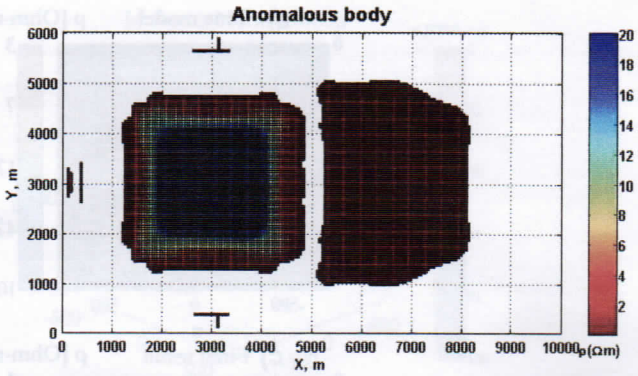

Figure 24 A plan view of the inverse model obtained by inversion of the synthetic MT data for Model 4.

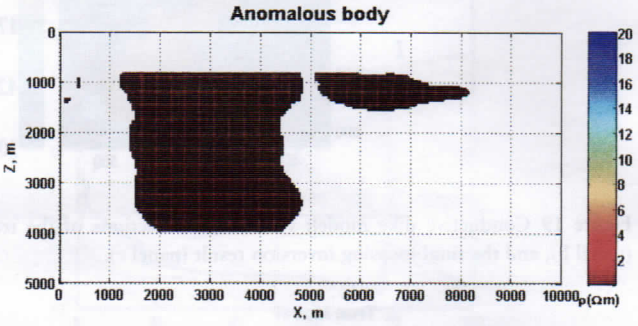

Figure 25 A side view of the inverse model obtained by inversion of the synthetic MT data for Model 4.

c and d present the corresponding predicted data. There is a very good fit between the observed and predicted data.

The corresponding MT sounding curves, computed for model 4 at an observation point close to the centre of the reservoir, are shown in Fig. 27. We can see that the observed and predicted data fit each other with a high degree of accuracy. Thus, the regularized focusing inversion provides an effective tool for practical interpretation of MT data.

CONCLUSIONS

The regularization is based, in general, on bringing the *a priori* information into the inverse problem solution. This information is included in the inversion by means of the appropriate choice of stabilizing functional. Until recently, only one type of regularization was widely used in practice – that based on the maximum smoothness criterion. The new regularized inversion technique discussed in this paper opens new frontiers for effective interpretation of geophysical data. In order to obtain a stable regularized solution, we can now consider different classes of inverse models, including an important

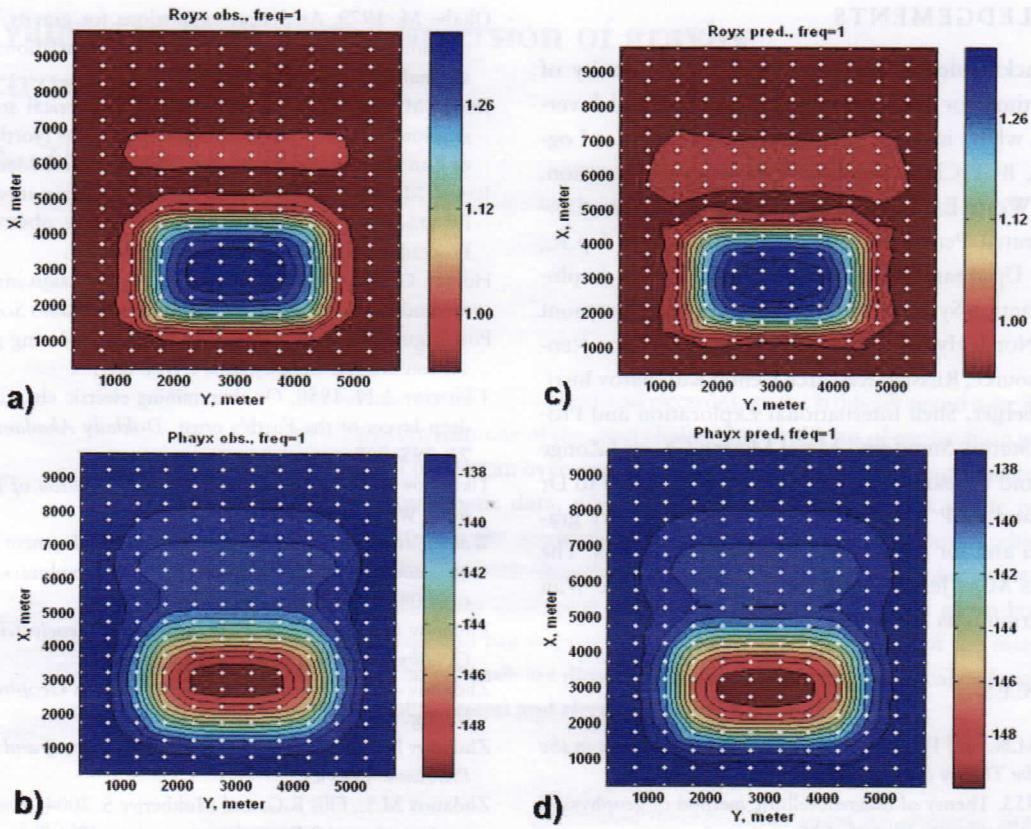

Figure 26 Maps of observed and predicted apparent resistivity and phase for Model 4. Panels a and b show the observed apparent resistivity and phase for *yx* polarization, while panels c and d present the corresponding predicted data.

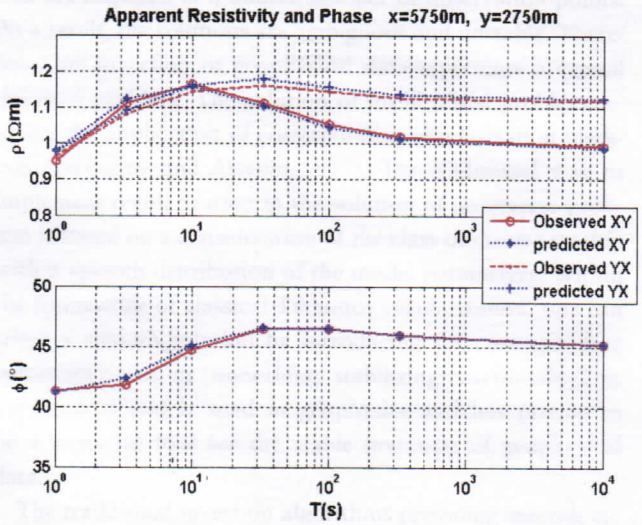

Figure 27 The observed and predicted MT sounding curves, Z_{xy} apparent resistivity and phase, for Model 4 at the point $x = 5,750$ m, and $y = 2,750$ m.

class of geological structures with sharp boundaries. This new approach provides more flexibility in the inversion of practical geophysical data.

Focusing inversion, similar to traditional smooth inversion, provides a regularized solution of the geophysical inverse problem. By choosing different types of stabilizing functionals, we can generate inversion images resolving different types of geological targets. In the case of a regional geophysical study, one can use a smooth inversion to recover the regional geological structures. In the exploration for local mining or petroleum targets, it is more appropriate to use focusing inversion, which allows us to determine the sharp petrophysical boundaries between the host rocks and the zones associated with a mineral deposit or a hydrocarbon reservoir. The final decision, which model to use for inversion – the one with a smooth distribution of physical properties or the one with the sharp boundaries – should be based on the analysis of all available geological information about the potential target of the geophysical exploration.

ACKNOWLEDGEMENTS

The author acknowledges the support of the University of Utah Consortium for Electromagnetic Modeling and Inversion (CEMI), which includes BAE Systems, Baker Atlas Logging Services, BGP China National Petroleum Corporation, BHP Billiton World Exploration Inc., British Petroleum, Centre for Integrated Petroleum Research, EMGS, Eni S.p.A., ExxonMobil Upstream Research Company, INCO Exploration, Information Systems Laboratories, MTEM, Newmont Mining Co., Norsk Hydro, OHM, Petrobras, Rio Tinto - Kennecott, Rocksource, Russian Research Center Kurchatov Institute, Schlumberger, Shell International Exploration and Production Inc., Statoil, Sumitomo Metal Mining Co. and Zonge Engineering and Research Organization. I am thankful to Dr Robert Ellis and BHP Billiton for providing the gravity gradiometer data and for permission to publish the results. The author thanks Mike Jessop, Ekaterina Tolstaya and Le Wan for their contributions in the numerical study.

REFERENCES

Berdichevsky M.N. and Dmitriev V.I. 2002. *Magnetotellurics in the Context of the Theory of Ill-posed Problems*. SEG.

Cagniard L. 1953. Theory of magnetotelluric method of geophysical prospecting. *Geophysics* **18**, 605–635.

Gribenko A. and Zhdanov M.S. 2007. Rigorous 3D inversion of marine CSEM data based on the integral equation method. *Geophysics* **72**, 229–254.

Okabe M. 1979. Analytical expressions for gravity anomalies due to homogeneous polyhedral bodies and translations into magnetic anomalies. *Geophysics* **64**, 730–741.

Jessop M. and Zhdanov M.S. 2005a. Numerical study of gravity gradiometer data for typical kimberlites in the Northwest Territory of Canada. Proceedings of 2005 CEMI Annual Meeting.

Jessop M. and Zhdanov M.S. 2005b. Focusing inversion of gravity gradient data collected on an arbitrary observation surface. Proceedings of 2005 CEMI Annual Meeting.

Hursán G. and Zhdanov M.S. 2002. Contraction integral equation method in 3-D electromagnetic modeling. *Radio Science* **37**, 1089.

Portniaguine O. and Zhdanov M.S. 1999. Focusing geophysical inversion images. *Geophysics* **64**, 874–887.

Tikhonov A.N. 1950. On determining electric characteristics of the deep layers of the Earth's crust. *Doklady Akadamia Nauk SSSR* **73**, 295–297.

Tikhonov A.N. and Arsenin V.Y. 1977. *Solution of Ill-posed Problems*. Winston and Sons.

Wan L. and Zhdanov M.S. 2004. New development in 3-D marine MT modeling and inversion for petroleum exploration. Proceedings of 2004 CEMI Annual Meeting.

Zhdanov M.S. and Keller G.W. 1994. *The Geoelectrical Methods in Geophysical Exploration*. Elsevier.

Zhdanov M.S. 1988. *Integral Transforms in Geophysics*. Springer-Verlag.

Zhdanov M.S. 2002. *Geophysical Inverse Theory and Regularization Problems*. Elsevier.

Zhdanov M.S., Ellis R.G. and Mukherjee S. 2004. Regularized focusing inversion of 3-D gravity tensor data. *Geophysics* **69**, 925–937.

Zhdanov M.S. and Tolstaya E. 2004. Minimum support nonlinear parameterization in the solution of 3-D magnetotelluric inverse problem. *Inverse Problems* **20**, 937–952.